RAA 2016 Vol. **16** No. **5**, 78 (12pp) doi: 10.1088/1674–4527/16/5/078
http://www.raa-journal.org *http://iopscience.iop.org/raa*

***R**esearch in*
***A**stronomy and*
***A**strophysics*

Investigation of intergranular bright points from the New Vacuum Solar Telescope

Kai-Fan Ji[1], Jian-Ping Xiong[1,2,3], Yong-Yuan Xiang[4], Song Feng[1,2,3], Hui Deng[1], Feng Wang[1,4] and Yun-Fei Yang[1,2,3] †

[1] Faculty of Information Engineering and Automation/Yunnan Key Laboratory of Computer Technology Application, Kunming University of Science and Technology, Kunming 650500, China; *yangyf@escience.cn*
[2] Key Laboratory of Solar Activity, National Astronomical Observatories, Chinese Academy of Sciences, Beijing 100012, China
[3] Key Laboratory of Modern Astronomy and Astrophysics, Nanjing University, Ministry of Education, Nanjing 210093, China
[4] Yunnan Observatories, Chinese Academy of Sciences, Kunming 650011, China

Received 2015 September 1; accepted 2015 November 30

Abstract Six high-resolution TiO-band image sequences from the New Vacuum Solar Telescope (NVST) are used to investigate the properties of intergranular bright points (igBPs). We detect the igBPs using a Laplacian and morphological dilation algorithm (LMD) and automatically track them using a three-dimensional segmentation algorithm, and then investigate the morphologic, photometric and dynamic properties of igBPs in terms of equivalent diameter, intensity contrast, lifetime, horizontal velocity, diffusion index, motion range and motion type. The statistical results confirm previous studies based on G-band or TiO-band igBPs from other telescopes. These results illustrate that TiO data from the NVST are stable and reliable, and are suitable for studying igBPs. In addition, our method is feasible for detecting and tracking igBPs with TiO data from the NVST. With the aid of vector magnetograms obtained from the Solar Dynamics Observatory/Helioseismic and Magnetic Imager, the properties of igBPs are found to be strongly influenced by their embedded magnetic environments. The areal coverage, size and intensity contrast values of igBPs are generally larger in regions with higher magnetic flux. However, the dynamics of igBPs, including the horizontal velocity, diffusion index, ratio of motion range and index of motion type are generally larger in the regions with lower magnetic flux. This suggests that the absence of strong magnetic fields in the medium makes it possible for the igBPs to look smaller and weaker, diffuse faster, and move faster and further along a straighter path.

Key words: techniques: image processing — Sun: photosphere — methods: data analysis — methods: statistical

1 INTRODUCTION

The New Vacuum Solar Telescope (NVST; Wang et al. 2013; Liu et al. 2014; Xu et al. 2014) at Fuxian Solar Observatory, administered by Yunnan Observatories in China, is designed to observe the Sun with very high spatial and spectral resolution in the wavelength range from 0.3 to 2.5 micron. Starting from October 2012, it has mainly provided Hα (656.3$\pm$0.025 nm) band data for observing the chromosphere and TiO (705.8$\pm$1 nm) band images for observing the photosphere. Many studies focusing on the small-scale structures and fine details in the chromosphere using Hα band data have been carried out (Yang et al. 2014a; Yang et al. 2014b; Bi et al. 2015; Yan et al. 2015; Yang et al. 2015a). However, studies using the TiO-band data are scarce.

Thought to be the footpoints of magnetic flux tubes, intergranular bright points (igBPs) are clearly visible in some lines formed in the photosphere, such as G-band, CN band, blue continuum and TiO-band (Zakharov et al. 2005; Abramenko et al. 2010). IgBPs show a strong spatial correlation with magnetic flux concentrations and are therefore useful as magnetic proxies, which allow the distribution and dynamics of magnetic features to be studied at a higher spatial resolution than using spectro-polarimetric techniques (Keller 1992; Berger & Title 2001; Sánchez Almeida 2001; Steiner et al. 2001; Schüssler et al. 2003; Carlsson et al. 2004; Shelyag et al. 2004; Beck et al. 2007; Ishikawa et al. 2007; de Wijn et al. 2008). A theoretical

† Corresponding author.

model for the formation process of igBPs is called the convective collapse model (Parker 1978; Spruit 1979). The model suggests that when the magnetic field exceeds an equipartition field strength, the plasmas within the magnetic field draught down, resulting in a small scale vertical flux tube that is visible as a bright point. The correlation between the brightness and the field strength is explained by a hot-wall mechanism (Spruit 1976; Spruit & Zwaan 1981). Accordingly, the less opaque magnetic flux-tube interior then causes an excess of lateral inflow of radiation into their evacuated interiors, and as a consequence the magnetic elements appear brighter than their surroundings. The radiative properties of igBPs possibly play an important role in influencing the Earth's climate (London 1994; Larkin et al. 2000; Gray et al. 2010; Ermolli et al. 2013; Solanki et al. 2013). Moreover, the motions of igBPs can influence the granulation and energy transport process in the lower solar atmosphere (e.g., a strong magnetic field can suppress normal convective flows; Title et al. 1989; Anđić et al. 2011). Therefore, the motions can indicate the properties of MHD waves excited in the lower solar atmosphere that may contribute to coronal heating, generate kinetic and Alfvén waves and then release energy (Roberts 1983; Parker 1988; Choudhuri et al. 1993; de Wijn et al. 2009; Jess et al. 2009; Zhao et al. 2009; Balmaceda et al. 2010; Ji et al. 2012).

In general, G-band (430.5 nm) and TiO-band (705.7 nm) observations are applied to study igBPs in previous works. Observations in G-band are regarded as an excellent proxy for studying igBPs because they appear brighter due to the reduced abundance of the CH molecule at higher temperatures (Steiner et al. 2001). Most studies of igBPs have been performed using different G-band observations, such as with the 48 cm Swedish Vacuum Solar Telescope (SVST; Berger et al. 1995; Berger et al. 1998; Berger & Title 2001), 43.8 cm Dutch Open Telescope (DOT; Bovelet & Wiehr 2003; Nisenson et al. 2003; de Wijn et al. 2005; Feng et al. 2013; Bodnárová et al. 2014), 1 m Swedish Solar Telescope (SST; Sánchez Almeida et al. 2004; Möstl et al. 2006; Chitta et al. 2012), 76 cm Dunn Solar Telescope (DST; Crockett et al. 2010; Keys et al. 2011; Romano et al. 2012; Keys et al. 2013; Keys et al. 2014); and seeing-free space-based 50 cm solar optical telescope onboard Hinode (SOT; Utz et al. 2009; Utz et al. 2010; Yang et al. 2014c; Yang et al. 2015b). Moreover, the TiO-band observation is also used to investigate the igBPs, e.g., the 1.6 m New Solar Telescope (NST; Abramenko et al. 2010; Abramenko et al. 2011). The TiO-band images provide an enhanced gradient of intensity around igBPs, which is very beneficial for imaging them. The reason for this is that the intensity for granules and igBPs is the same as observed in the continuum, whereas for dark cool intergranular lanes, the observed intensity is lowered due to absorption in the TiO line since this spectral line is sensitive to temperature (Abramenko et al. 2010). In spite of different diffraction limits of these telescopes, the statistical properties of igBPs have been agreed as follows: the typical equivalent diameter is about 150 km, which corresponds to a range of igBP equivalent diameters of 76 to 400 km; the typical ratio of the maximum intensity of igBP to the mean photospheric intensity is about 1.1, corresponding to a range of 0.8 to 1.8; the mean lifetime is several minutes, corresponding to a range of $2-20$ min; the mean horizontal velocity is $1-2\,\mathrm{km\ s^{-1}}$ with a maximum value of $7\,\mathrm{km\ s^{-1}}$; the mean diffusion index ranges from 0.7 to 1.8.

In the last few decades, the properties of igBPs in quiet Sun (QS) regions and active regions (ARs) have been compared using observational data. For instance, Romano et al. (2012) indicated that igBPs in a QS region are brighter and smaller than those in an AR, but Feng et al. (2013) drew a different conclusion. Most authors agreed that the dynamics of igBPs are attenuated in ARs compared to QS regions (Berger et al. 1998; Möstl et al. 2006; Keys et al. 2011). Keys et al. (2014) defined one QS sub-region and two active sub-regions in the same field of view (FOV) judging by their mean line-of-sight magnetic flux densities. They proposed that the size of igBPs in the QS region is smaller and the horizontal velocity is greater. Besides observations, Crockett et al. (2010) utilized mean magnetic fields of 100 G, 200 G and 300 G in the magnetohydrodynamic simulations and compared the igBP size with the DST observations. They suggested that the igBP size does not significantly depend on the embedded magnetic environments. Criscuoli (2013) also analyzed results from simulations characterized by different amounts of average magnetic flux. They indicated that the igBPs decrease in terms of intensity contrast with increasing environmental magnetic flux. However, few works have been carried out from observations to investigate the differences in the properties of igBPs embedded in varying magnetic fluxes.

The aim of this paper is to investigate the igBPs using the TiO-band data observed from the NVST. Six high-resolution image sequences are selected that span the time from 2012 to 2014, and have different heliocentric angles and magnetic fluxes. We detect and track the igBPs automatically, and investigate the morphologic, photometric and dynamic properties of igBPs, in terms of equivalent diameter, intensity contrast, lifetime, horizontal velocity, diffusion index, motion range and motion type. In addition, we investigate the relation between the igBP properties and the amount of magnetic flux in the region in which they are embedded. The layout of this paper is as follows: observations and data reductions are described in Section 2. The method is detailed in Section 3. In Section 4, the statistics of igBPs in different magnetized environments are presented and discussed, followed by the conclusion in Section 5.

2 OBSERVATIONS AND DATA REDUCTIONS

The NVST is a vacuum solar telescope with a 985 mm clear aperture, which is designed to observe multi-wavelength data with high spatial and spectral resolution. It uses a broadband TiO filter centered at a wavelength of

705.8 nm for observing the photosphere. The team provides the level 1^+ data, which are processed by frame selection (lucky imaging; Tubbs 2004), and reconstructed by speckle masking (Lohmann et al. 1983) or iterative shift and add (Zhou & Li 1998). The reconstructed images under the best seeing conditions can almost have a high angular resolution near the diffraction limit of the NVST (105 km) even without the adaptive optics system (Liu et al. 2014). We selected six high-resolution image sequences under the best seeing conditions that were acquired without the adaptive optics system from October 2012 to October 2014. Then, six sub-regions with equal dimensions ($20'' \times 20''$) were extracted from the six data sets, respectively. The observational parameters are listed in Table 1. Note that the pixel sizes of the data sets after 2014 are different because the NVST team changed their optical system on 2014 May 19 and this resulted in the difference. The images in each sequence were aligned by a sub-pixel level image registration procedure (Feng et al. 2012; Yang et al. 2015b). The projection effects of the data sets that are away from the solar disk center were corrected according to the heliocentric longitude and latitude of each pixel.

In order to investigate and compare the properties of igBPs embedded in regions characterized by different average values of magnetic flux, we used the vector magnetograms observed with the Helioseismic and Magnetic Imager (HMI; Schou et al. 2012) onboard the Solar Dynamics Observatory (SDO; Pesnell et al. 2012). The HMI data were processed with the standard hmi_prep routine in SolarSoftware. With the aid of the HMI continuum images, the TiO-band images were co-aligned with the vector magnetograms by a sub-pixel registration algorithm (Feng et al. 2012; Yang et al. 2015b) and the subfields were chosen from the vector magnetograms. Subsequently, the co-aligned sub-magnetograms during the observed time interval of each data set were averaged to improve their sensitivity to the mean magnetic flux density. The data sets are listed in Table 1 in the order of corresponding mean magnetic flux density, B. Figures 1 and 2 show two data sets with the lowest and highest B, which were recorded on 2013 May 21 and 2012 October 29, respectively.

3 METHODS

A Laplacian and morphological dilation algorithm (LMD; Feng et al. 2013) was used to detect the igBPs in each image. The algorithm consists of three main steps: first, the smoothed TiO image is convolved with a Laplacian in an operation to yield a Laplacian image; second, a threshold of μ+3σ is applied to the Laplacian image to produce a binary image, where the μ and σ are the mean value and the standard deviation of the Laplacian image, respectively; finally, the igBPs are filtered by selecting the features whose lengths of the edges are 70 percent inside the intergranular lanes as determined from the binary image. Two samples of the identified igBPs are marked with white in Figure 1(b) and Figure 2(b).

After detecting the igBPs in each image, a three-dimensional (3D) segmentation algorithm (Yang et al. 2014c) was employed to track the evolution of igBPs in the image sequence. The image sequence is regarded as a 3D space-time cube (x, y, z), in which the x and y axes are the two dimensional image coordinates, and the z axis represents the frame index of the image sequence. Based on a 26-adjacent technique (Yang et al. 2013; Yang et al. 2014c), the evolution of an igBP presents a 3D structure in a 3D space-time cube. Figure 3 shows two samples of the 3D space-time cubes of data sets 1 and 6.

The isolated igBPs that do not merge or split during their lifetimes are selected here because their size, intensity, lifetime and velocity are clearly defined. We also discard the isolated igBPs with incomplete life cycles or lifetimes that are less than 100 s. The remaining igBPs (isolated igBPs with complete life cycles) are the focus of this study.

Table 2 lists the total numbers of igBPs, non-isolated igBPs, isolated igBPs with incomplete life cycles and isolated igBPs with complete life cycles.

4 RESULTS AND DISCUSSION

4.1 Statistical Properties of igBPs

The areal coverage is defined as the percentage of the fractional area occupied by igBPs. The values of the six data sets are listed in Table 3. They range from 0.2% to 2%, which is consistent with most previous studies of 0.5%–3% (see Table 4). After that, we calculated the properties of igBPs in terms of equivalent diameter, intensity contrast, lifetime, horizontal velocity, diffusion index, motion range and motion type. The equivalent diameter is calculated with $\sqrt{4A/\pi}$, where A denotes the area of an igBP. The intensity contrast is defined as the ratio of the peak intensity of an igBP to the average intensity of a quiet subregion. The lifetime is determined by the number of frames over its corresponding 3D structure. The horizontal velocity is calculated by the displacement of the two centroids between successive frames of an igBP, whose centroid is the arithmetic mean position of all the pixels in the shape of an igBP in a frame. The other properties will be detailed below. Table 3 lists the mean values, standard deviations and ranges of all igBP properties for each data set.

Figure 4 only illustrates the histograms and the best fitted curves of data sets 1 and 6 since their mean magnetic flux densities are the lowest and highest respectively among all six data sets. The lines represent the histograms (dashed) and the distribution curves (solid) corresponding to data set 1. The dash-dotted and dotted lines represent the same shapes corresponding to data set 6. The other data sets have similar distributions and fitted curves.

Figure 4(a) shows the distributions of equivalent diameters of igBPs and fitted lines from a log-normal curve. The log-normal distribution of the igBP diameters is consistent with the suggestion that the process of fragmentation and merging dominate the process of flux concentra-

Table 1 The Parameters of Six Data Sets

Data set	Date	Time interval (UT)	Center of the FOV ($''$)	Pixel size ($''$)	Cadence (s)	B (G)[1]
1	2013–05–21	06:14:05–07:30:50	(–232, 358)	0.041	55	94
2	2013–06–12	07:45:34–09:07:29	(–173, –170)	0.041	55	127
3	2014–10–03	04:35:50–05:25:32	(25, –108)	0.052	30	143
4	2013–07–15	07:29:09–08:22:22	(285, –313)	0.041	40	169
5	2014–09–13	02:29:23–03:19:06	(–445, 126)	0.052	30	191
6	2012–10–29	06:03:37–06:43:25	(–436, –279)	0.041	40	229

Notes: [1] B: Mean magnetic flux density.

Table 2 The Numbers of IgBPs in the Six Data Sets

Data set	1	2	3	4	5	6
Total igBPs	170	506	1190	991	2071	1177
Non-isolated igBPs	59	223	506	218	464	308
Isolated igBPs with incomplete life cycles	9	13	39	66	79	77
Isolated igBPs with complete life cycles	102	270	645	707	1528	792
Non-stationary isolated igBPs with complete life cycles	75	190	440	290	625	337

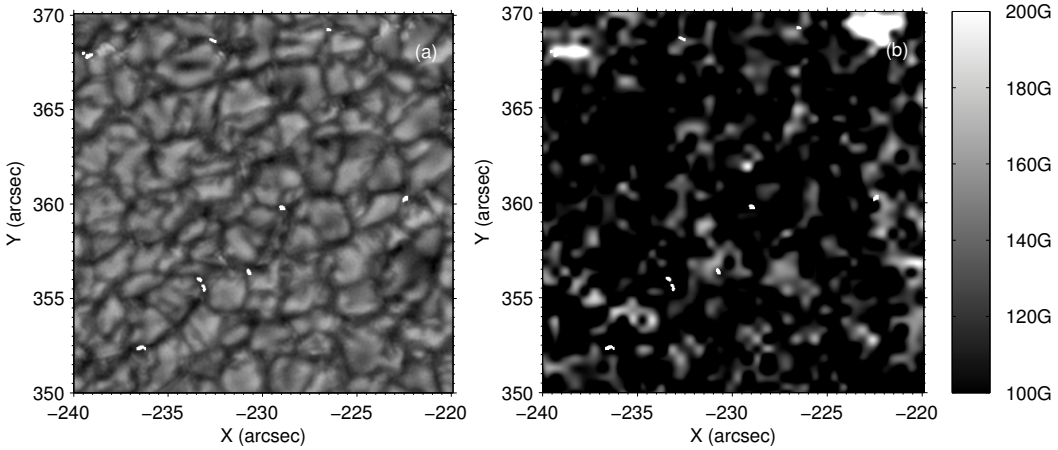

Fig. 1 (a) One TiO-band image was recorded at 06:14:05 UT on 2013 May 21 from the NVST, in which the detected igBPs are marked with white. (b) The co-spatial HMI vector magnetogram, in which the mean magnetic flux density is 94 G and the maximum value is 321 G. The detected igBPs are also marked with white. The color bar in (b) indicates the magnetic flux density saturated at [100, 200] G to assist visualization of the field complexities. The axes are in units of arcseconds from the solar disk center.

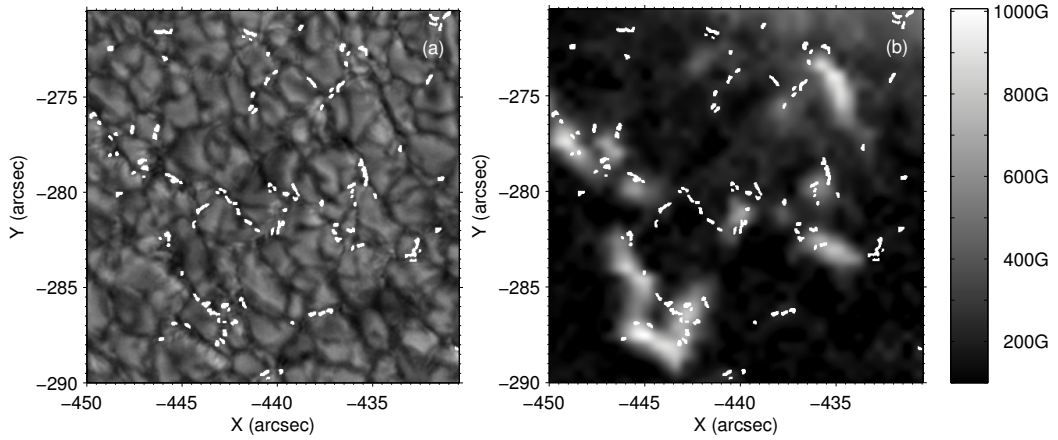

Fig. 2 (a) One TiO-band image was recorded at 06:03:37 UT on 2012 October 29 from the NVST, in which the detected igBPs are marked with white. (b) The co-spatial HMI vector magnetogram, the mean magnetic flux density of which is 228 G and the maximum value is 1006 G. The detected igBPs are also marked with white. The color bar in (b) indicates the magnetic flux density, saturated at [100, 1006] G. The axes are in units of arcseconds from the solar disk center.

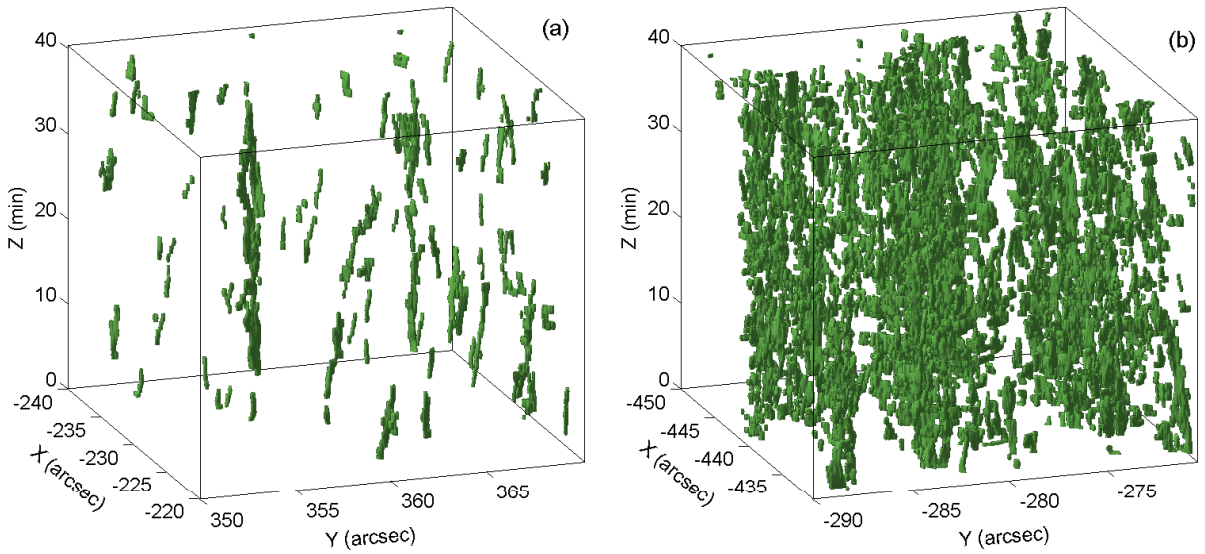

Fig. 3 (a) One segment of the 3D space-time cube whose size is $20'' \times 20'' \times 40$ min from data set 1. The x and y axes correspond to those in Fig. 1(a), and the z axis represents the time interval from 06:14:05 UT to 06:54:05 UT. (b) One segment of the 3D space-time cube showing igBPs whose size is $20'' \times 20'' \times 40$ min of data set 6. The x and y axes correspond those in Fig. 2(a), and the z axis represents the time interval from 06:03:37 UT to 06:43:37 UT. The evolution of an igBP is displayed as a 3D structure in the 3D space-time cube.

Table 3 The Properties of IgBPs from the Six Data Sets

Data set	1	2	3	4	5	6
Areal coverage	0.20%	0.99%	1.55%	1.53%	1.75%	1.99%
Equivalent diameter (km)	181±22	168±29	178±29	195±36	184±38	194±36
[*min,max*]	[*111, 245*]	[*103, 402*]	[*109, 440*]	[*106, 445*]	[*122, 447*]	[*112, 473*]
Intensity contrast	0.99±0.04	1.01±0.04	1.03±0.04	1.05±0.06	1.05±0.04	1.06±0.05
[*min,max*]	[*0.91, 1.12*]	[*0.90, 1.19*]	[*0.90, 1.31*]	[*0.92, 1.30*]	[*0.92, 1.24*]	[*0.89, 1.28*]
Lifetime (sec)	104±104	133±133	114±114	141±141	121±121	124±124
[*min,max*]	[*103, 582*]	[*102, 826*]	[*120, 723*]	[*119, 735*]	[*120, 572*]	[*114, 580*]
Velocity (km s^{-1})	1.35±0.71	1.23±0.64	1.06±0.55	1.04±0.54	1.06±0.55	1.05±0.55
[*min,max*]	[*0.01, 5.27*]	[*0, 6.80*]	[*0.08, 5.43*]	[*0.02, 5.32*]	[*0.06, 5.21*]	[*0.03, 5.75*]
Diffusion index	1.31±0.65	1.21±0.78	0.91±0.43	1.05±0.67	0.86±0.49	0.93±0.77
[*min,max*]	[*–3.64, 3.93*]	[*–4.91, 5.39*]	[*–4.17, 4.28*]	[*–5.21, 6.51*]	[*–7.00, 4.21*]	[*–5.70, 4.43*]
Ratio of motion range	1.30±0.80	1.18±0.76	1.11±0.77	1.02±0.62	0.96±0.67	1.03±0.69
[*min,max*]	[*0.31, 5.06*]	[*0.15, 6.39*]	[*0.04, 6.28*]	[*0.17, 5.42*]	[*0.13, 4.73*]	[*0.13, 4.79*]
Motion type	0.69±0.69	0.69±0.69	0.58±0.58	0.59±0.59	0.59±0.59	0.62±0.62
[*min,max*]	[*0.08, 0.99*]	[*0.04, 1.00*]	[*0.23, 0.99*]	[*0.03, 0.99*]	[*0, 1.00*]	[*0.04, 0.98*]

Table 4 The Areal Coverage of the IgBPs from Some Previous Studies

Reference	Telescope	Region	Magnetic fluxes	Spatial resolution ($''$)	Temporal resolution (s)	Areal coverage
Berger et al. (1995)	SVST	AR		0.083		1.8%
Feng et al. (2013)	DOT	QS		0.071	30	0.5%
Feng et al. (2013)	DOT	AR		0.071	30	1.4%
Sánchez Almeida et al. (2004)	SST	QS	0.9 G	0.041	15	0.5%−0.7%
Sánchez Almeida et al. (2010)	SST	QS	29 G	0.041	15	0.9%−2.2%
Romano et al. (2012)	SST	QS		0.041	89	0.8%
Romano et al. (2012)	SST	AR		0.041	20	1.9%

tion (Abramenko & Longcope 2005). The distribution of data set 1 is sharper than that of data set 6. The mean values and the standard deviations of data sets 1 and 6 are 182±22 and 194±36 km, respectively. For all of the six data sets, the mean diameters range from 168 to 195 km (see Table 3). All of the minimum values saturate at scales corresponding to the diffraction limit of NVST, which is 105 km in the TiO-band. The maximum value of data set 1 is 245 km, which is smaller than those of other data sets. We found that the isolated igBPs of data set 1 are nearly circular in shape, while some of the other data sets form chains that result in a relatively large equivalent diame-

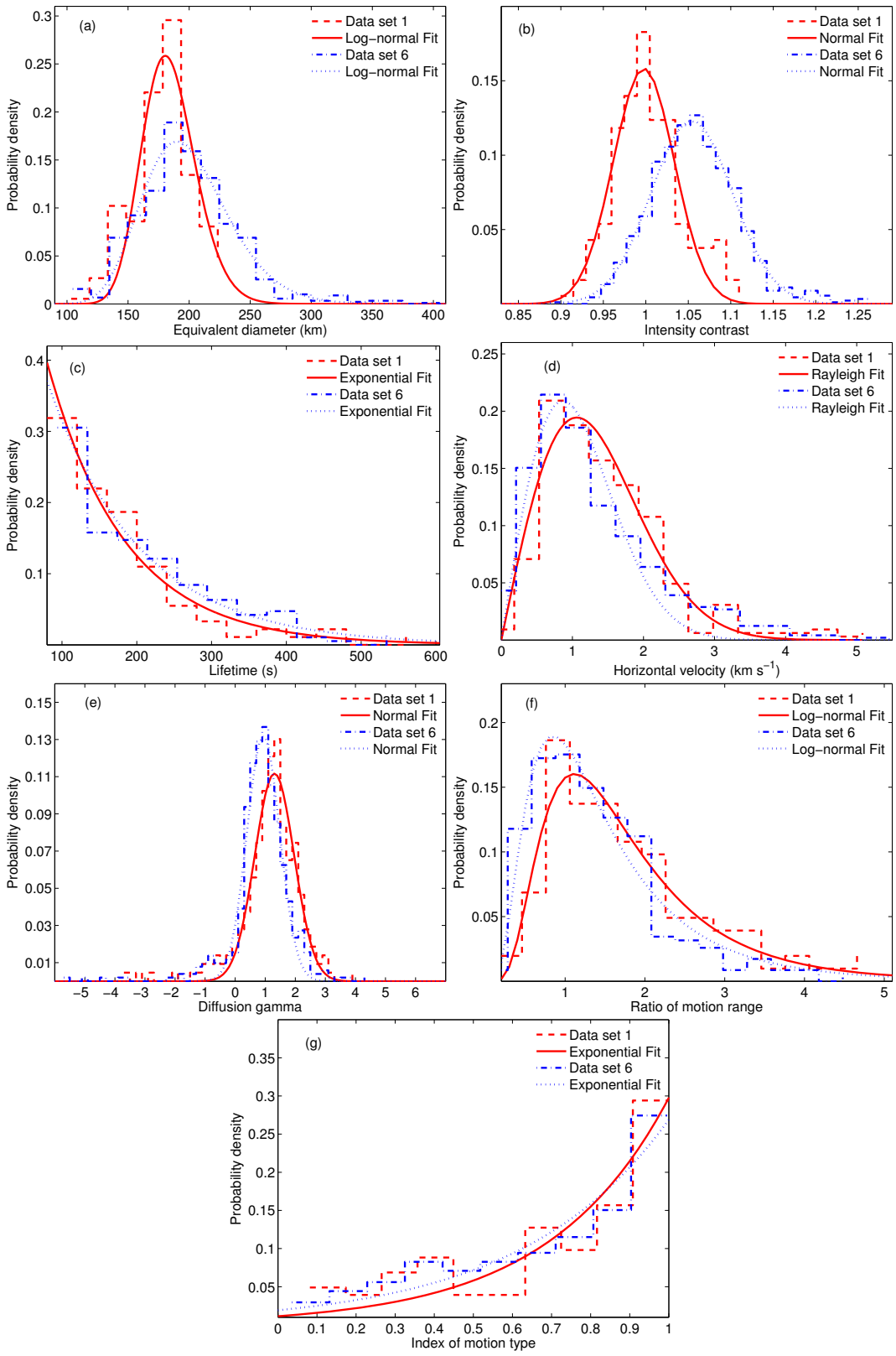

Fig. 4 The histograms and fitted curves of igBP properties associated with data sets 1 and 6. The lines represent the histograms (*dashed*) and distribution curves (*solid*) of the properties of data set 1. The dash-dotted and dotted lines represent the corresponding shapes of data set 6. (a) equivalent diameter; (b) the intensity contrast; (c) lifetime; (d) horizontal velocity; (e) diffusion index; (f) the ratio of motion range; and, (g) the index of motion type.

ter. These results are consistent with previous studies (see Table 5). All of the authors agreed that the minimum size of igBPs has not yet been detected in observations with modern high resolution telescopes and the maximum size cannot be larger than the characteristic width of the intergranular lanes.

Figure 4(b) shows distributions of the intensity contrast of igBPs and fitted lines from a normal curve. The distribution of data set 1 is sharper than that of data set 6. The mean values and standard deviations of data sets 1 and 6 are 0.99±0.04 and 1.06±0.05, respectively. It can be seen in Table 3 that the mean values of all the data sets range from 0.99 to 1.06, and the minimum value and the maximum value are 0.89 and 1.31, respectively. Previous studies concluded that the intensity contrast of G-band igBPs is 0.8-1.8 (see Table 6). Both the minimum values are about 0.8, but the maximum value of TiO-band data is much less than 1.8. This implies that the intensity contrast of the TiO-band igBPs is lower than G-band igBPs.

Figure 4(c) shows the distributions of the lifetime of igBPs and fitted lines from an exponential curve. The distributions indicate that most igBPs have a short lifetime. The mean values of these similar distributions are 104 and 124 s, respectively. Note that the standard deviation of an exponential function is the same as its mean value.

From Table 3, it can be found that values of the mean lifetime of all data sets range from 104 to 141 s, and the maximum value reaches 826 s. Our results are consistent with most previous studies listed in Table 7. However, some authors obtained a long value of lifetime, e.g., Berger et al. (1998) and Nisenson et al. (2003). Berger et al. (1998) measured the mean lifetime for all igBPs including isolated and non-isolated igBPs. The lifetimes of non-isolated igBPs are generally long because they undergo numerous split or merge interactions. For the six data sets, the maximum lifetime of non-isolated igBPs is 59 min. Nisenson et al. (2003) only measured the igBPs whose lifetimes are longer than 210 s. Here, we measured the lifetimes of isolated igBPs with lifetime > 100 s.

Figure 4(d) shows the distributions of all the calculated horizontal velocities between successive frames of igBPs. The horizontal velocities in the x and the y directions are both fitted to a normal function well. Therefore, the distribution of rms horizontal velocities fits the Rayleigh function well. The distribution of data sets 6 is sharper than that of data set 1, which is different in terms of equivalent diameters and the intensity contrast. The mean values and the standard deviations of data sets 1 and 6 are 1.35±0.71 and 1.05±0.55 km s^{-1}, respectively. For all of the data sets, the mean values range from 1.04 to 1.35 km s^{-1}, which confirm the previous studies (see Table 8).

Figure 4(e) shows the distributions of the diffusion index, γ, and fitted lines from the normal curve. Diffusion processes represent the efficiency of dispersal in the photosphere, which uses a diffusion index to quantify the transport process with respect to a normal diffusion (random walk). A diffusion process can be characterized by the relation $(\Delta l)^2 = C\tau^{\gamma}$, where Δl represents the displacement of an igBP between its location at given time τ and its initial location; γ is the diffusion index and C is a constant of proportionality (Dybiec & Gudowska-Nowak 2009; Jafarzadeh et al. 2014; Yang et al. 2015c). Diffusions with $\gamma < 1$, $\gamma = 1$ and $\gamma > 1$ are called sub-diffusive, normal-diffusive and super-diffusive, respectively. The γ value of each igBP was measured by the slope of the square of its displacement on a log-log scale, where the time scale is determined by its lifetime. Subsequently, we obtained the mean value for γ and the standard deviation by curve fitting the histogram of all γ values. The distributions are fitted to a normal function well. As a result, the mean values of γ for data sets 1 and 6 are 1.31±0.65 and 0.93±0.77, respectively. It can also be seen that the mean values of the six data sets range from 0.86 to 1.31 in Table 3. It is worth noting that γ values less than 0 are meaningless. If an igBP moves in an erratic or circular path, the slope of the linear fit on a log-log scale would be below 0 or very large with a low goodness-of-fit (Yang et al. 2015c). The results are in agreement with most previous studies (see Table 9). The authors got the range of diffusion index from 0.76 to 1.79. It implies that igBPs in different magnetic regions have various regimes, such as sub-, normal- and super-diffusive regimes. IgBPs in strong magnetic fields are crowded within narrow intergranular lanes when compared with a weak magnetic environment, where igBPs can move freely due to a lower population density (Abramenko et al. 2011). This is the main reason that igBPs in a weaker magnetic region diffuse faster than those in a stronger one.

Figure 4(f) shows the distributions of the ratio of motion range of igBPs and fitted curves from the log-normal curve. The range for the rate of motion is defined as $m_r = \sqrt{(X_{\max} - X_{\min})^2 + (Y_{\max} - Y_{\min})^2}/r$, where $X_{\max}$ and $X_{\min}$ are the maximum and minimum coordinates of the path of a single igBP on the x axis respectively, and $Y_{\max}$ and $Y_{\min}$ are the corresponding values on the y axis; r is the radius of the circle which corresponds to the maximum size of the igBP during its lifetime (Bodnárová et al. 2014; Yang et al. 2015b). If the m_r value of an igBP is less than 1, the igBP moves within its own maximum radius during its lifetime. Such an igBP is called stationary. Otherwise, an igBP with $m_r \geq 1$ is called non-stationary. The numbers of non-stationary igBPs of the six data sets are listed in Table 2. The percents of the non-stationary igBPs range from 40% to 73%. Bodnárová et al. (2014) and Yang et al. (2015b) both found that the m_r values of about 50% of igBPs are less than 1 from QS observations. We believe that our wide-ranging results are caused by the different magnetic environments. Moreover, the mean m_r values and the standard deviations of data set 1 and data set 6 are 1.30±0.80 and 1.03±0.69, and the maximum m_r values are 5.06 and 4.79, respectively.

From Table 3, the mean values of the six data sets range from 0.96 to 1.30, which implies that igBPs move nearly as far as the associated radius. The maximum values of the six data sets range from 4.73 to 6.39, which are

Table 5 The Diameters of IgBPs from Some Previous Studies

Reference	Telescope	Region	Spatial resolution ($''$)	Temporal resolution (s)	Mean diameter (km)
Berger et al. (1995)	SVST	AR	0.083		250
Bovelet & Wiehr (2003)	DOT	AR	0.071	30	220±25
Feng et al. (2013)	DOT	QS	0.071	30	224±40
Feng et al. (2013)	DOT	AR	0.071	30	232 ±45
Crockett et al. (2010)	DST	QS	0.069	2	230
Utz et al. (2009)	SOT	QS	0.054	30	166±31
Utz et al. (2009)	SOT	QS	0.108	30	218±48
Romano et al. (2012)	SST	QS	0.041	89	216
Romano et al. (2012)	SST	AR	0.041	20	268
Abramenko et al. (2010)	NST	QS	0.0375	10	77−260

Notes: The range of igBP diameters.

Table 6 The Intensity Contrasts of IgBPs from Some Previous Studies

Reference	Telescope	Region	Magnetic fluxes	Spatial resolution ($''$)	Temporal resolution (s)	Mean intensity contrast
Feng et al. (2013)	DOT	QS		0.071	30	1.3
Feng et al. (2013)	DOT	AR		0.071	30	1.6
Utz et al. (2013)	SOT	QS		0.108	30	1.0
Utz et al. (2013)	SOT	AR		0.108	30	1.4
Yang et al. (2014c)	SOT	QS		0.054	30	1.02±0.11
Sánchez Almeida et al. (2004)	SST	QS	0.9 G	0.041	15	0.8−1.8
Möstl et al. (2006)	SST	AR		0.041	20	1.17±0.08
Romano et al. (2012)	SST	QS		0.041	20	1.09±0.05
Romano et al. (2012)	SST	AR		0.041	20	1.05±0.06

Table 7 The Lifetimes of IgBPs from Some Previous Studies

Reference	Telescope	Region	Magnetic fluxes	Spatial resolution ($''$)	Temporal resolution (s)	Mean lifetime (s)
Berger et al. (1998)	SVST	QS		0.083	23	560
Nisenson et al. (2003)	DOT	Network		0.071	30	552
de Wijn et al. (2005)	DOT	Network		0.071	30	210
Keys et al. (2014)	DST	QS	3 G	0.069	2	88±23
Keys et al. (2014)	DST	AR	169 G	0.069	2	136±40
Utz et al. (2010)	SOT	QS		0.054	30	150±5
Möstl et al. (2006)	SST	AR		0.041	20	260±137
Abramenko et al. (2010)	NST	QS		0.0375	10	120−720

consistent with the previous studies that obtained a value of about 7 (Bodnárová et al. 2014; Yang et al. 2015b).

Figure 4(g) shows the distributions of the index of motion type of igBPs and fitted lines from the exponential curve. Putting aside the stationary igBPs, we focus on the motion type of the non-stationary cases. The index of motion type is defined as $m_t = d/L$, where $d = \sqrt{(X_n - X_1)^2 + (Y_n - Y_1)^2}$; here (X_1, Y_1) is the start location and (X_n, Y_n) is the final location during its lifetime; L is the whole path length, defined as $L = \sum_{t=1}^{n-1} \sqrt{\Delta X_t^2 + \Delta Y_t^2}$; here $\Delta X_t = X_{t+1} - X_t$, $\Delta Y_t = Y_{t+1} - Y_t$. It is a ratio of the displacement of an igBP to its whole path length (Yang et al. 2015b). According to the definition, the m_t value must be between 0 and 1. If an igBP moves in a nearly straight line, the m_t value will be close to 1. But if it moves in a nearly closed curve, then the m_t value will be close to 0. The motion types of non-straight lines are referred to as erratic motion type. Please refer to Yang et al. (2015b) for details. We found that the distributions of m_t values fit an exponential function well. The m_t values of half of igBPs from data set 1 and 6 are greater than 0.75 and 0.68, respectively. About 25% and 29% igBPs of data sets 1 and 6 have m_t values that are less than 0.5, respectively. The mean values are 0.69 and 0.62, respectively. The mean m_t values of the six data sets range from 0.58 to 0.69. The distribution of m_t is very similar to that analyzed by Yang et al. (2015b). They indicated that the m_t values of half of the igBPs are larger than 0.83 and 15% are less than 0.5.

We applied different curve fitting functions to determine the analytical fit for the distribution functions of the properties of igBPs, such as normal, log-normal, exponential and Rayleigh. The parameter of Adjusted R-squared indicates how successful the fit is in explaining the variation of the data (Cameron & Windmeijer 1997). Consequently, we adopted the functions with the highest Adjusted R-squared values: normal function for intensity contrasts and diffusion indices, log-normal for equivalent diameters and

Table 8 The Horizontal Velocities of IgBPs from Some Previous Studies

Reference	Telescope	Region	Magnetic fluxes	Spatial resolution ($''$)	Temporal resolution (s)	Mean horizontal velocity (km s^{-1})
Berger et al. (1998)	SVST	QS		0.083	23	1.1
Berger et al. (1998)	SVST	AR		0.083	23	0.95
Nisenson et al. (2003)	DOT	Network		0.071	30	0.89
Keys et al. (2014)	DST	QS	3 G	0.069	2	0.9±0.4
Keys et al. (2014)	DST	AR	169 G	0.069	2	0.6±0.3
Utz et al. (2010)	SOT	QS		0.054	30	1.62±0.05
Möstl et al. (2006)	SST	AR		0.041	20	1.11

Table 9 The Diffusion Indices of IgBPs from Some Previous Studies

Reference	Telescope	Region	Magnetic fluxes	Spatial resolution ($''$)	Temporal resolution (s)	Mean diffusion index
Cadavid et al. (1999)	SVST	Network		0.083	23	0.76±0.04/1.10±0.24
Keys et al. (2014)	DST	QS	3 G	0.069	2	1.21±0.25
Keys et al. (2014)	DST	AR	169 G	0.069	2	1.23±0.22
Yang et al. (2015c)	SOT	QS		0.108	30	1.79±0.01
Yang et al. (2015c)	SOT	AR		0.108	30	1.53±0.01
Abramenko et al. (2011)	NST	coronal hole		0.0375	10	1.67
Abramenko et al. (2011)	NST	QS		0.0375	10	1.53
Abramenko et al. (2011)	NST	plage area		0.0375	10	1.48

Notes: for time intervals of 0.3−22 min / for 25−57 min.

the ratios of motion range, exponential for lifetimes and the indices of motion type, and Rayleigh for horizontal velocities. These distribution functions are consistent with most of the previous works cited above.

4.2 Relation between igBP Properties and Magnetic Field

It can be seen that the statistical values of igBPs in the six magnetic environments are different in Table 3 and Figure 4. In order to explore the relations between the properties of igBPs and their embedded magnetic environments, Figure 5 shows the correlations between the mean magnetic flux density of the region in which igBPs are embedded and igBP properties of the six data sets, in terms of areal coverage, diameter, intensity contrast, lifetime, horizontal velocity, diffusion index, the ratio of motion range and the index of motion type. The box and the solid line are the mean value and the standard error of each data set, respectively. The dashed line is the linear fit of the data points. The relations of areal coverage-magnetic flux density, diameter-magnetic flux density and intensity contrast-magnetic flux density show a positive correlation with correlation coefficients of 0.77, 0.64 and 0.94, respectively. The relations of horizontal velocity-magnetic flux density, diffusion index-magnetic flux density, the ratio of motion range-magnetic flux density and the index of motion type-magnetic flux density show a negative correlation with correlation coefficients of –0.81, –0.79, –0.87 and –0.60, respectively. However, the lifetime-magnetic flux density relation fails to exhibit an obvious correlation with a correlation coefficient of 0.39.

Our results are in good qualitative agreement with most previous studies in Tables 4 – 9. It implies that in a higher magnetic environment, the igBP is larger and brighter, and its movement is attenuated (e.g. the lower horizontal velocity, sub-diffusion, limited motion range and erratic type motion). These different physical properties result from the inhibition of convection induced by the presence of the magnetic field, which changes the temperature stratification of both quiet and magnetic regions (Criscuoli 2013). Note that we found that the intensity contrast of igBPs in a higher magnetic environment is larger than that in a lower magnetic environment. The result is consistent with Feng et al. (2013) and Utz et al. (2013), but differs from Romano et al. (2012). Additionally, the previous studies suggested that the igBPs live longer in stronger magnetic environments (Keys et al. 2014), however, our results did not show an obvious relation for the embedded magnetic environment.

5 CONCLUSIONS

Six high-resolution TiO-band image sequences which span the years from 2012 to 2014 were obtained under excellent seeing conditions from the New Vacuum Solar Telescope (NVST) at Fuxian Solar Observatory, administered by Yunnan Astronomical Observatory, China. We investigate the morphologic, photometric and dynamic properties of igBPs, in terms of equivalent diameter, intensity contrast, lifetime, horizontal velocity, diffusion index, motion range and motion type. With the aid of vector magnetograms obtained with the SDO/HMI, the statistical properties of igBPs in different magnetic environments are also explored and compared.

The statistics of igBPs indicate that the quality of the TiO-band data from the NVST is stable and reliable. The areal coverages of igBPs range from 0.2% to 2%. The mean equivalent diameters range from 168±29 to

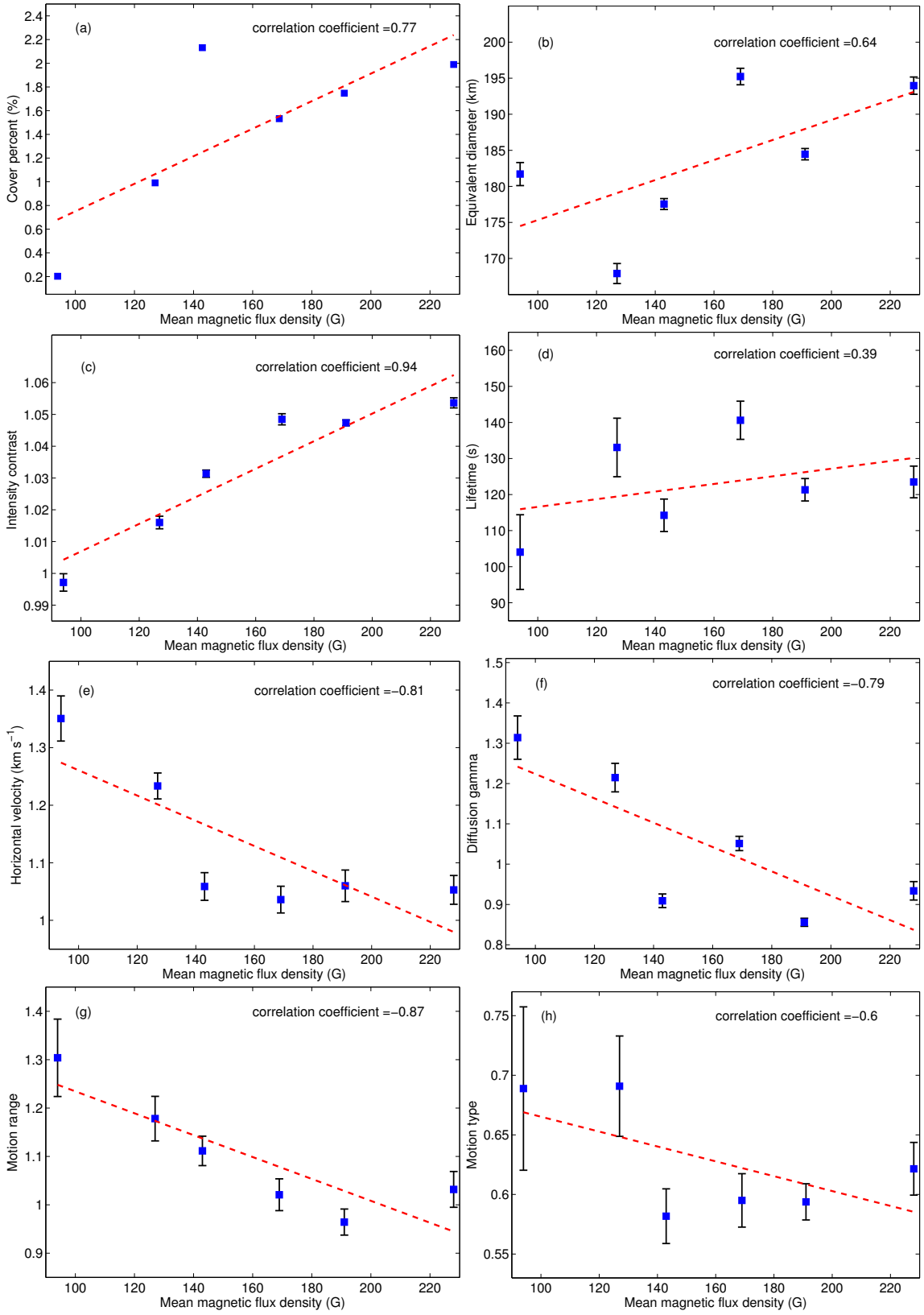

Fig. 5 The relation plots between the mean magnetic flux density and the igBP properties: (a) areal coverage-mean magnetic flux density; (b) diameter-mean magnetic flux density; (c) intensity contrast-mean magnetic flux density; (d) lifetime-mean magnetic flux density; (e) horizontal velocity-mean magnetic flux density; (f) diffusion gamma-mean magnetic flux density; (g) the ratio of motion range-mean magnetic flux density; and (h) the index of motion type-mean magnetic flux density. The boxes and the solid lines are the mean values and the standard errors of the igBP property for each data set, respectively. The dashed lines are the associated linear fits.

195±36 km. The mean ratios of intensity contrast range from 0.99±0.04 to 1.06±0.05. The mean lifetimes range from 104 to 141 s. The mean horizontal velocities range from 1.04±0.54 to 1.35±0.71 km s^{-1}. The mean diffusion indices range from 0.86±0.39 to 1.31±0.54. Values of the mean ratio of motion range from 0.96±0.67 to 1.30±0.80, and values of the mean index of motion type range from 0.58 to 0.69. Moreover, the mean values and the standard deviations of igBP properties are consistent with previously published studies based on G-band or TiO-band observations from other telescopes, such as SVST, DOT, DST, SOT, SST and NST. It implies that the TiO-band data from the NVST are very suitable for studying the igBPs, and the LMD and three-dimensional segmentation algorithms are feasible for detecting and tracking igBPs from the TiO-band acquired by the NVST.

In addition, different magnetic environments are considered, and are characterized by different mean magnetic flux density. Values for the areal coverage, size and intensity contrast of igBPs are generally larger in the regions of high magnetic flux. However, the dynamics of igBPs, in terms of horizontal velocity, diffusion index, ratio of motion range and index of motion type are generally larger in regions with low magnetic flux. Previous studies focused on comparing the properties of igBPs in the QS and AR, or different sub-regions in the same FOV. This study provides further information about the relation between the properties of igBPs and their embedded magnetic environments based on six data sets that span three years, which are located in different solar positions and have different magnetic fluxes. This suggests that the stronger magnetic field makes the igBPs look bigger and brighter, and attenuates their movements (e.g. lower horizontal velocity, subdiffusion, limited motion range and erratic type motion).

Acknowledgements The authors are grateful to the anonymous referee for constructive comments and detailed suggestions on this manuscript. The authors are grateful for the support received from the National Natural Science Foundation of China (Nos. 11573012, 11303011, 11263004, 11163004 and U1231205) and the Open Research Program of the Key Laboratory of Solar Activity of the Chinese Academy of Sciences (Nos. KLSA201414 and KLSA201505). The authors thank the NVST team for their high-resolution observations and level 1^+ data. The HMI data used here are courtesy of NASA/SDO and the HMI science teams.

References

Abramenko, V. I., Carbone, V., Yurchyshyn, V., et al. 2011, ApJ, 743, 133
Abramenko, V. I., & Longcope, D. W. 2005, ApJ, 619, 1160
Abramenko, V., Yurchyshyn, V., Goode, P., & Kilcik, A. 2010, ApJ, 725, L101
Anđić, A., Chae, J., Goode, P. R., et al. 2011, ApJ, 731, 29
Balmaceda, L., Vargas Domínguez, S., Palacios, J., Cabello, I., & Domingo, V. 2010, A&A, 513, L6
Beck, C., Bellot Rubio, L. R., Schlichenmaier, R., & Sütterlin, P. 2007, A&A, 472, 607
Berger, T. E., Löfdahl, M. G., Shine, R. A., & Title, A. M. 1998, ApJ, 506, 439
Berger, T. E., Schrijver, C. J., Shine, R. A., et al. 1995, ApJ, 454, 531
Berger, T. E., & Title, A. M. 2001, ApJ, 553, 449
Bi, Y., Jiang, Y., Yang, J., et al. 2015, ApJ, 805, 48
Bodnárová, M., Utz, D., & Rybák, J. 2014, Sol. Phys., 289, 1543
Bovelet, B., & Wiehr, E. 2003, A&A, 412, 249
Cadavid, A. C., Lawrence, J. K., & Ruzmaikin, A. A. 1999, ApJ, 521, 844
Cameron, A. C., & Windmeijer, F. A. 1997, Journal of Econometrics, 77, 329
Carlsson, M., Stein, R. F., Nordlund, Å., & Scharmer, G. B. 2004, ApJ, 610, L137
Chitta, L. P., van Ballegooijen, A. A., Rouppe van der Voort, L., DeLuca, E. E., & Kariyappa, R. 2012, ApJ, 752, 48
Choudhuri, A. R., Auffret, H., & Priest, E. R. 1993, Sol. Phys., 143, 49
Criscuoli, S. 2013, ApJ, 778, 27
Crockett, P. J., Mathioudakis, M., Jess, D. B., et al. 2010, ApJ, 722, L188
de Wijn, A. G., Lites, B. W., Berger, T. E., et al. 2008, ApJ, 684, 1469
de Wijn, A. G., McIntosh, S. W., & De Pontieu, B. 2009, ApJ, 702, L168
de Wijn, A. G., Rutten, R. J., Haverkamp, E. M. W. P., & Sütterlin, P. 2005, A&A, 441, 1183
Dybiec, B., & Gudowska-Nowak, E. 2009, Phys. Rev. E, 80, 061122
Ermolli, I., Matthes, K., Dudok de Wit, T., et al. 2013, Atmospheric Chemistry & Physics, 13, 3945
Feng, S., Deng, L., Shu, G., et al. 2012, in Advanced Computational Intelligence (ICACI), 2012 IEEE Fifth International Conference on, 626
Feng, S., Deng, L., Yang, Y., & Ji, K. 2013, Ap&SS, 348, 17
Gray, L. J., Beer, J., Geller, M., et al. 2010, Reviews of Geophysics, 48, 4001
Ishikawa, R., Tsuneta, S., Kitakoshi, Y., et al. 2007, A&A, 472, 911
Jafarzadeh, S., Cameron, R. H., Solanki, S. K., et al. 2014, A&A, 563, A101
Jess, D. B., Mathioudakis, M., Erdélyi, R., et al. 2009, Science, 323, 1582
Ji, H., Cao, W., & Goode, P. R. 2012, ApJ, 750, L25
Keller, C. U. 1992, Nature, 359, 307
Keys, P. H., Mathioudakis, M., Jess, D. B., Mackay, D. H., & Keenan, F. P. 2014, A&A, 566, A99
Keys, P. H., Mathioudakis, M., Jess, D. B., et al. 2013, MNRAS, 428, 3220
Keys, P. H., Mathioudakis, M., Jess, D. B., et al. 2011, ApJ, 740, L40

Larkin, A., Haigh, J. D., & Djavidnia, S. 2000, Space Sci. Rev., 94, 199
Liu, Z., Xu, J., Gu, B.-Z., et al. 2014, RAA (Research in Astronomy and Astrophysics), 14, 705
Lohmann, A. W., Weigelt, G., & Wirnitzer, B. 1983, Appl. Opt., 22, 4028
London, J. 1994, Advances in Space Research, 14, 33
Möstl, C., Hanslmeier, A., Sobotka, M., Puschmann, K., & Muthsam, H. J. 2006, Sol. Phys., 237, 13
Nisenson, P., van Ballegooijen, A. A., de Wijn, A. G., & Sütterlin, P. 2003, ApJ, 587, 458
Parker, E. N. 1978, ApJ, 221, 368
Parker, E. N. 1988, ApJ, 330, 474
Pesnell, W. D., Thompson, B. J., & Chamberlin, P. C. 2012, Sol. Phys., 275, 3
Roberts, B. 1983, Sol. Phys., 87, 77
Romano, P., Berrilli, F., Criscuoli, S., et al. 2012, Sol. Phys., 280, 407
Sánchez Almeida, J. 2001, ApJ, 556, 928
Sánchez Almeida, J., Bonet, J. A., Viticchié, B., & Del Moro, D. 2010, ApJ, 715, L26
Sánchez Almeida, J., Márquez, I., Bonet, J. A., Domínguez Cerdeña, I., & Muller, R. 2004, ApJ, 609, L91
Schou, J., Borrero, J. M., Norton, A. A., et al. 2012, Sol. Phys., 275, 327
Schüssler, M., Shelyag, S., Berdyugina, S., Vögler, A., & Solanki, S. K. 2003, ApJ, 597, L173
Shelyag, S., Schüssler, M., Solanki, S. K., Berdyugina, S. V., & Vögler, A. 2004, A&A, 427, 335
Solanki, S. K., Krivova, N. A., & Haigh, J. D. 2013, ARA&A, 51, 311
Spruit, H. C. 1976, Sol. Phys., 50, 269
Spruit, H. C. 1979, Sol. Phys., 61, 363
Spruit, H. C., & Zwaan, C. 1981, Sol. Phys., 70, 207
Steiner, O., Hauschildt, P. H., & Bruls, J. 2001, A&A, 372, L13
Title, A. M., Tarbell, T. D., Topka, K. P., et al. 1989, ApJ, 336, 475
Tubbs, R. N. 2004, The Observatory, 124, 159
Utz, D., Hanslmeier, A., Möstl, C., et al. 2009, A&A, 498, 289
Utz, D., Hanslmeier, A., Muller, R., et al. 2010, A&A, 511, A39
Utz, D., Jurčák, J., Hanslmeier, A., et al. 2013, A&A, 554, A65
Wang, R., Xu, Z., Jin, Z.-Y., et al. 2013, RAA (Research in Astronomy and Astrophysics), 13, 1240
Xu, Z., Jin, Z. Y., Xu, F. Y., & Liu, Z. 2014, in IAU Symposium, 300, eds. B. Schmieder, J.-M. Malherbe, & S. T. Wu, 117
Yan, X. L., Xue, Z. K., Pan, G. M., et al. 2015, ApJS, 219, 17
Yang, S., Zhang, J., Liu, Z., & Xiang, Y. 2014a, ApJ, 784, L36
Yang, S., Zhang, J., & Xiang, Y. 2014b, ApJ, 793, L28
Yang, S., Zhang, J., & Xiang, Y. 2015a, ApJ, 798, L11
Yang, Y.-F., Lin, J.-B., Feng, S., et al. 2014c, RAA (Research in Astronomy and Astrophysics), 14, 741
Yang, Y.-F., Qu, H.-X., Ji, K.-F., et al. 2015b, RAA (Research in Astronomy and Astrophysics), 15, 569
Yang, Y., Ji, K., Feng, S., et al. 2015c, ApJ, 810, 88
Yang, Y., Lin, J., & Deng, L. 2013, in Intelligent Networks and Intelligent Systems (ICINIS), 2013 6th International Conference on, IEEE, 304
Zakharov, V., Gandorfer, A., Solanki, S. K., & Löfdahl, M. 2005, A&A, 437, L43
Zhao, M., Wang, J.-X., Jin, C.-L., & Zhou, G.-P. 2009, RAA (Research in Astronomy and Astrophysics), 9, 933
Zhou, L., & Li, C.-S., eds. 1998, Society of Photo-Optical Instrumentation Engineers (SPIE) Conference Series, 3561, Electronic Imaging and Multimedia Systems II